Supporting Information

YAP-dependent Mechanotransduction is Required for Proliferation and Migration on Native-like Substrate Topography

Shamik Mascharak, Patrick L. Benitez, Amy C. Proctor, Christopher M. Madl, Kenneth H. Hu, Ruby E. Dewi, Prof. Manish J. Butte, Prof. Sarah C. Heilshorn[*]

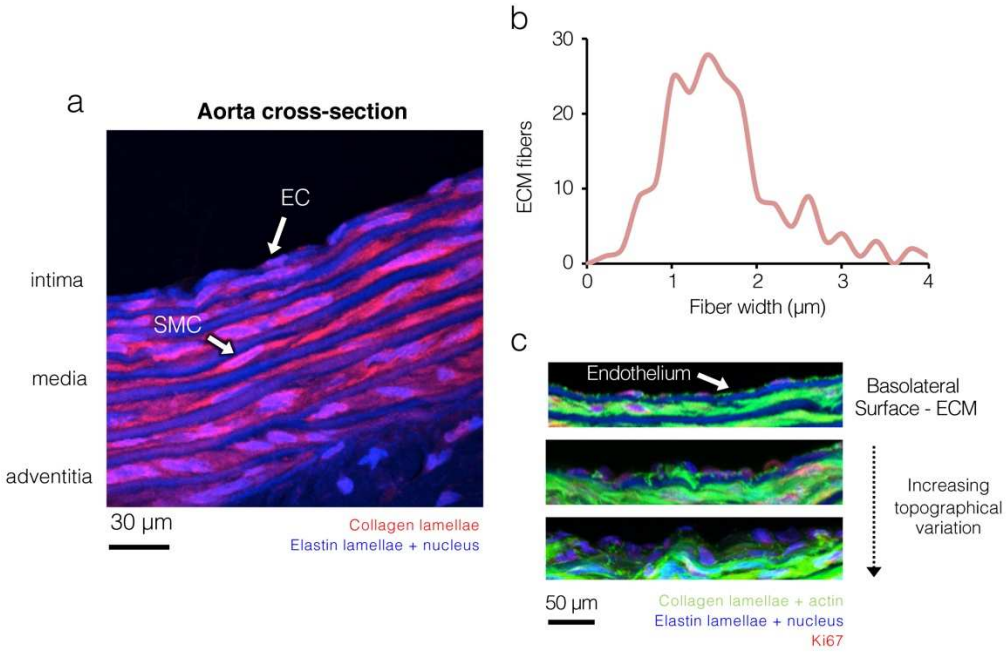

Figure S1. Micron-scale topographical variation occurs *in vivo*. a) Aortic cross-section labeled for cell nuclei (blue), collagen (red), and elastin lamellae (autofluorescent blue). Endothelial cells in the intimal layer were closely associated with the internal elastic lamina, supporting the use of an elastin-like sequence to recapitulate native mechanics. b) Histogram of *in vivo* fiber widths quantified using aortic cross sections from 5 rats. We observed native fibers with widths ranging from hundreds of nanometers to 4 µm with an average value of ~1.5 µm, a similar range to the fiber widths achieved in this study. c) Aortic cross-sections labeled for actin (green), Ki67 (red), nuclei (blue), and elastin/collagen lamellae (autofluorescent blue and green, respectively). The basolateral surface directly below the EC monolayer visibly followed the native topographical variation. Calculation across all specimens yielded an average arc-chord ratio of 1.6, well within the range of arc-chord ratios achieved in our electrospun ELP system (1.2 – 1.8).

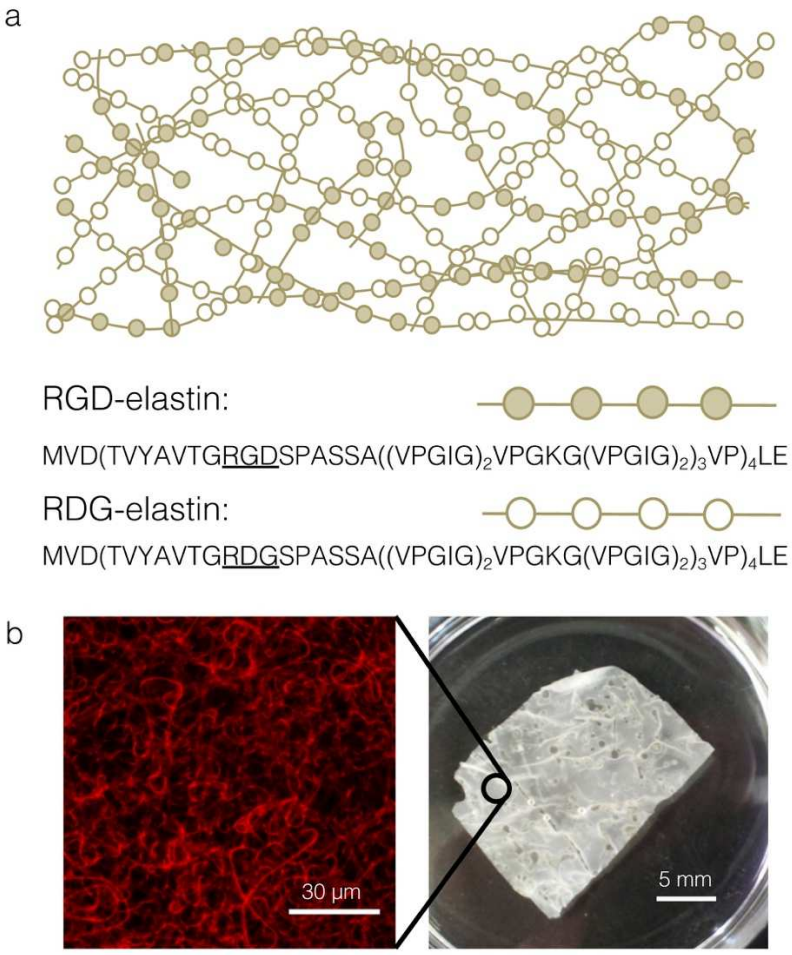

Figure S2. Electrospun ELP features native-like and tunable mechanics, biochemistry, and fibrous microtopography. a) Elastin-like proteins (ELP) containing either RGD ligands or scrambled RDG non-ligands were blended in a 13:87 mass ratio before electrospinning to specify global RGD concentration at 18 ligands per 1000 μm^2. Top schematic illustrates distribution of RGD (tan) and RDG (white) groups within individual fibers. b) Left: Crosslinked and hydrated ELP matrices feature micron scale fibrous topography, as observed by confocal microscopy of autofluorescent fibers. Right: ELP fabrics can be made as free-standing materials.

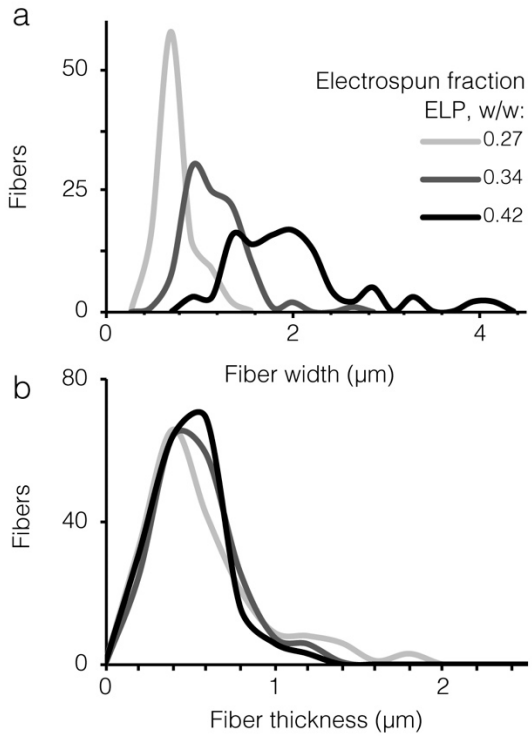

Figure S3. ELP fiber width is tuned by specifying total protein mass fraction in the precursor spinning solution. a,b) Histograms of ELP fiber widths and heights for precursor electrospinning solutions with 27, 34, and 42% w/w ELP). Increasing total ELP mass fraction yielded wider (0.8, 1.2, and 2.0 μm) but not thicker (~500 nm) fibers, consistent with prior results (Benitez *et al*. *Adv Healthcare Mat* **2**, 114-118; 2013). Fiber width distributions were significantly different by ANOVA with Tukey-Kramer *post-hoc* test.

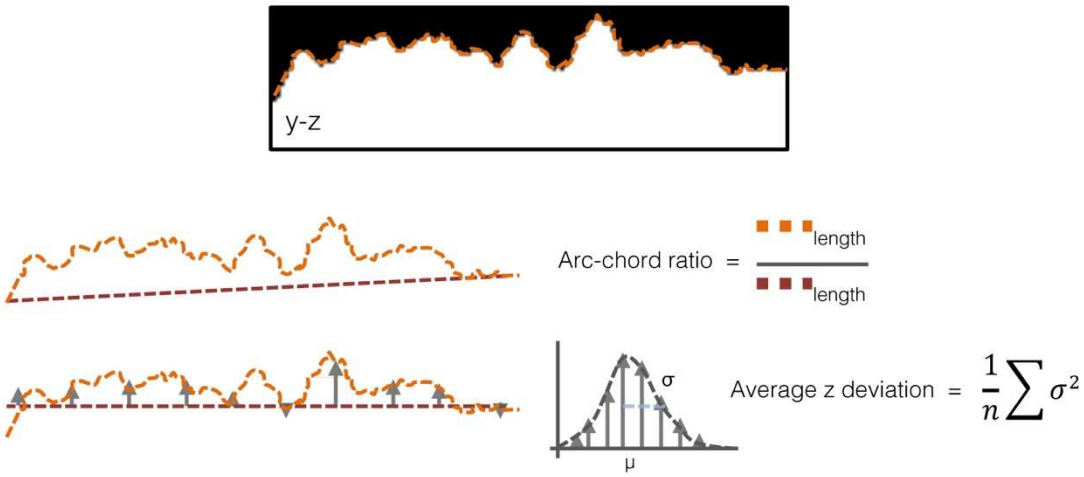

Figure S4. Arc-chord ratio and average z deviation are two parameters to quantify topographical variation. Top: Arc-chord ratio is calculated from orthogonal projections by dividing the contour length of the material interface (shown in orange) by the end-to-end displacement length (shown in red). Bottom: Average z deviation (shown as a gray arrow) is calculated by measuring the distance between the material interface (shown in orange) and the mean z value (shown in red). The variances of the z distance distributions (σ^2) are then averaged.

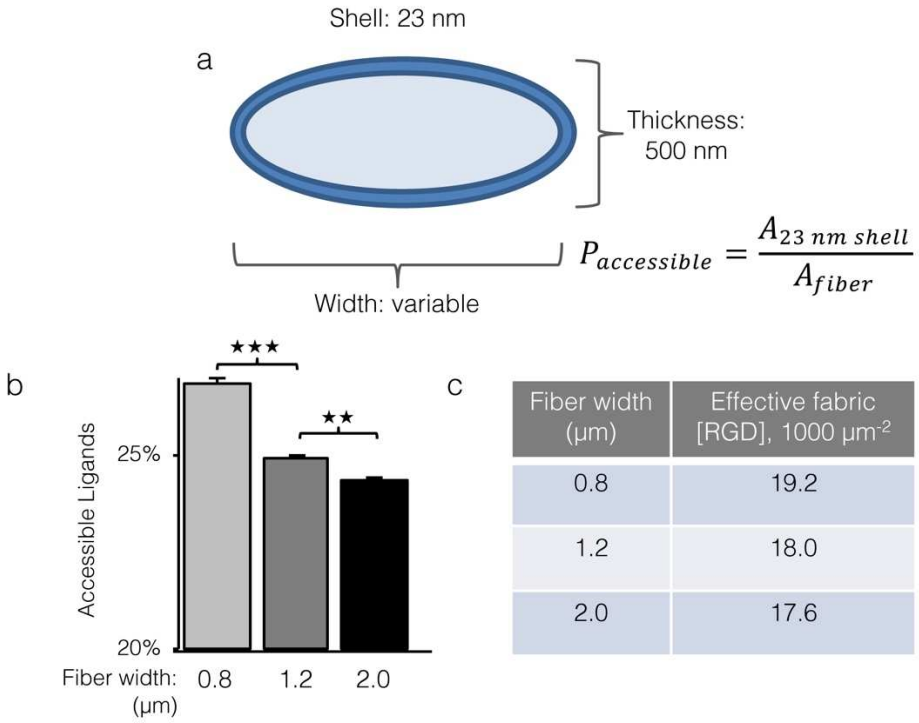

Fiber width (μm)	Effective fabric [RGD], 1000 μm^{-2}
0.8	19.2
1.2	18.0
2.0	17.6

Figure S5. Increasing fiber width did not cause a biologically significant change in accessible RGD ligands. a) Representation of an ELP fiber cross-section. The proportion of total RGD ligands that are accessible to a cell ($P_{accessible}$) was estimated as the area of a 23-nm shell (corresponding to the extracellular length of an $\alpha_v\beta_3$ integrin) divided by the total fiber cross-sectional area. b) A significant but small (~3%) decrease in accessible ligands was noted between 0.8 and 1.2 μm wide fibers. This change was not expected to be biologically relevant given previous data of ECs on ELP fabrics (Benitez *et al*. *Integr*. *Biol*. **8**, 50-61; 2015). c) Table of estimated effective RGD concentrations for each fabric; see Experimental Section for sample calculations. (** $p < 0.01$, *** $p < 0.001$)

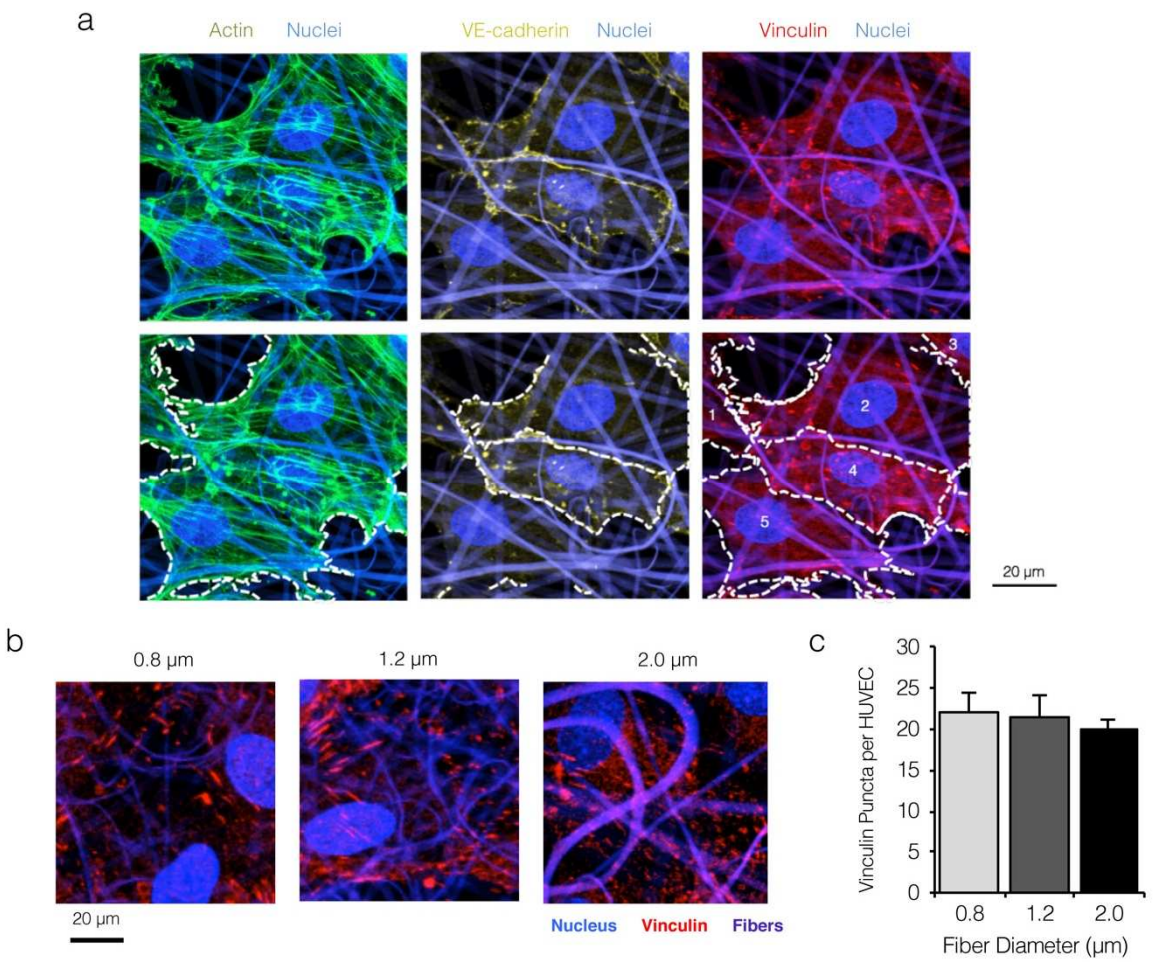

Figure S6. Increasing fiber width did not cause a change in focal adhesion distribution. a) ECs cultured on topographically varied substrate ELP fabrics (2.0 μm fibers) and immunostained for VE-cadherin (yellow), actin (green), and the nucleus (blue). Fibers are shown in blue. Actin staining defined cell-matrix borders (bottom left), while the VE-cadherin staining defined cell-cell junctions (bottom middle). Taken together, these borders defined the total area of each cell (bottom right) and distinguished focal adhesions from different cells. b) ECs cultured on varied width ELP matrices and immunostained for the focal adhesion adaptor protein vinculin (green), actin (red), and the nucleus (blue). Fibers are shown in violet. c) Quantification of vinculin puncta per cell (see Experimental Section). The number of focal adhesions per cell did not vary with fiber width, supporting our prediction of no biologically significant shift in accessible RGD ligand content.

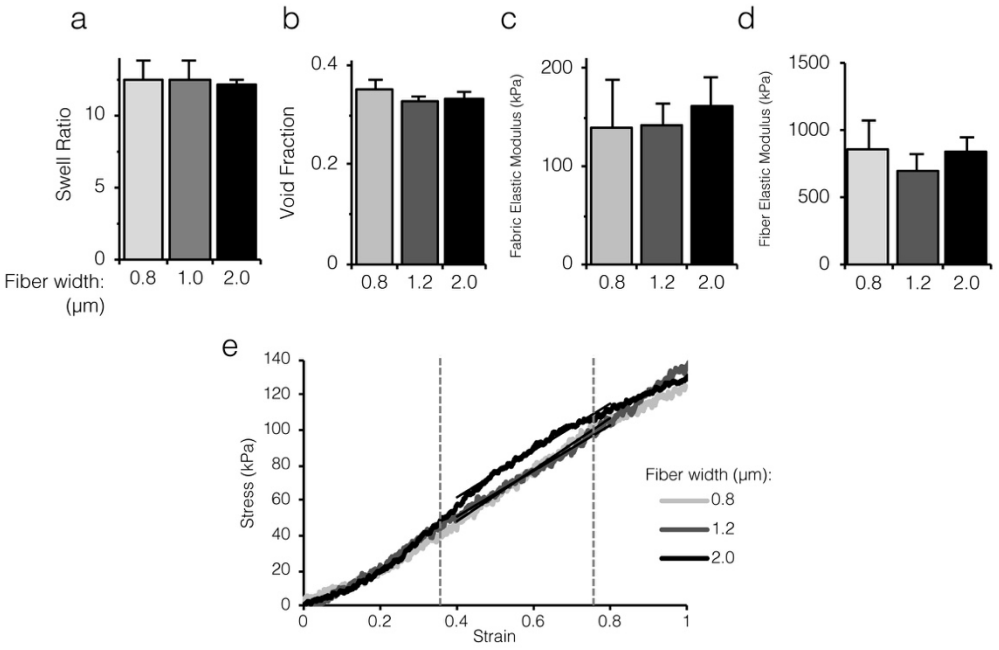

Figure S7. Key bulk biomaterial properties are not significantly altered by increasing fiber width. a) Swell ratio for electrospun ELP matrices did not vary significantly with fiber width, implying a similar volume density of protein. b) Void fraction also did not vary with fiber width. Together with the unchanging swell ratio, this implied that aqueous buffer content was similar across samples. c,d) Bulk and individual fiber elastic moduli for ELP matrices did not vary with fiber width. Thus, independent tuning of topographical and mechanical properties was achieved at all length scales.

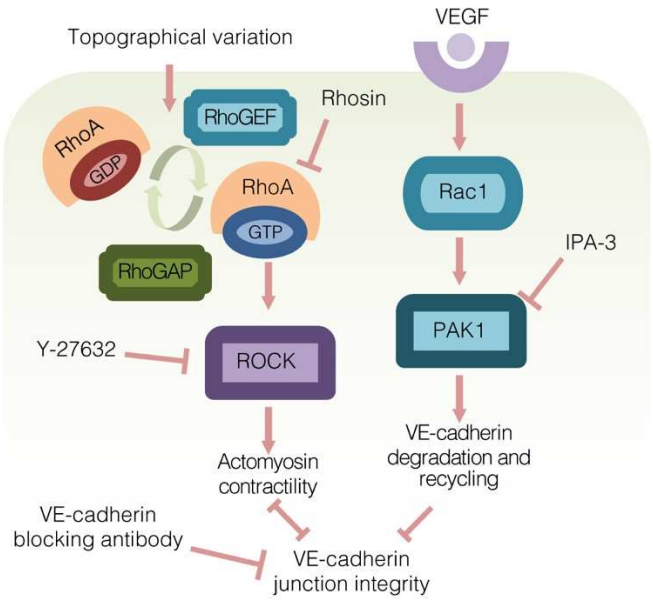

Figure S8. Explanatory schematic: Interactions between VE-cadherin and the actin cytoskeleton. Under quiescent conditions, actin stress fibers are arranged parallel to the cell cortex. Stimulation of the endothelium (in this case by topographical variation) induces perpendicular reorganization of actin filaments and contractility via Rho/ROCK signaling, thereby decreasing VE-cadherin junction integrity. An alternate pathway also exists, whereby Rac1/PAK1 activation (for example, by vascular endothelial growth factor (VEGF)) promotes VE-cadherin degradation and recycling. In this study, we employ three different inhibitors, Y-27632, Rhosin, and IPA-3, to block signaling by ROCK, Rho, and Rac, respectively.

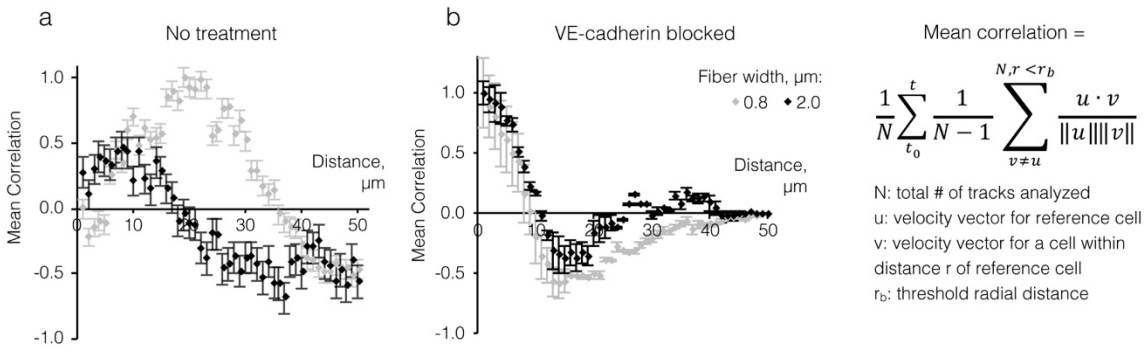

Figure S9. Spatial correlation plots indicated decreased contact guidance by VE-cadherin on larger width ELP matrices. a) Spatial correlation (see formula to the right) between velocity vectors decreased quickly for ECs on more varied topography. The radial distance for which mean correlation between velocity vectors equals 0 was taken to be the correlation distance. b) Spatial correlation decreased quickly for ECs on all topographies after VE-cadherin blocking. This indicated that decreased cell-cell coordination on wider fibers was specifically due to loss of VE-cadherin.

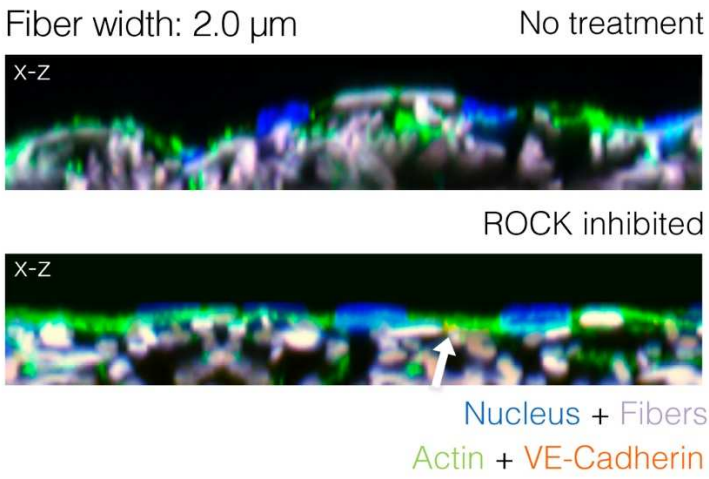

Figure S10. Cytoskeletal inhibition blocked EC curvature over fibers. Orthogonal projections of ECs cultured on the widest fiber condition (2.0 μm) and stained for actin (green), VE-cadherin (red), and nuclei (blue). Fibers are shown in white. While untreated ECs curved to follow the contours of the topographical features, ROCK-inhibited ECs displayed a flat, planar basolateral membrane with strong adherens junctions (white arrow).

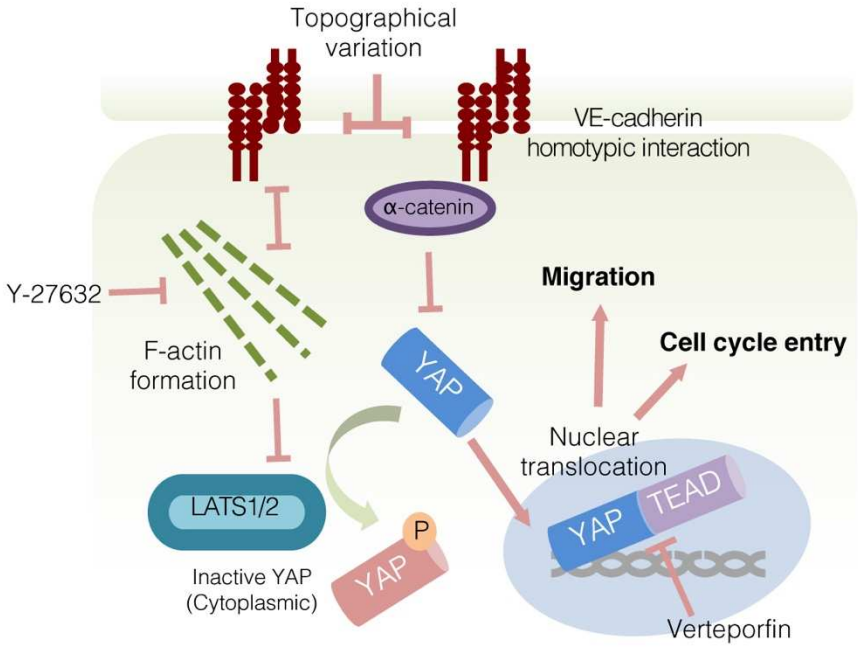

Figure S11. Explanatory schematic: Mechanistic hypothesis linking topographical variation to migration and cell cycle entry via YAP activation. Yes-associated protein (YAP) mediates endothelial quiescence in concert with VE-cadherin through two separate pathways. In the first pathway, catenins associated with VE-cadherin at mature adherens junctions induce phosphorylation (inactivation) of cytoplasmic YAP. In the second pathway, VE-cadherin suppresses F-actin formation and contractility, which in turn disinhibits LATS1/2. Disinhibited LATS1/2 phosphorylates and inactivates cytoplasmic YAP. We hypothesized that topography-mediated disruption of VE-cadherin would prevent inactivation of YAP by these two pathways, thereby promoting YAP nuclear translocation.

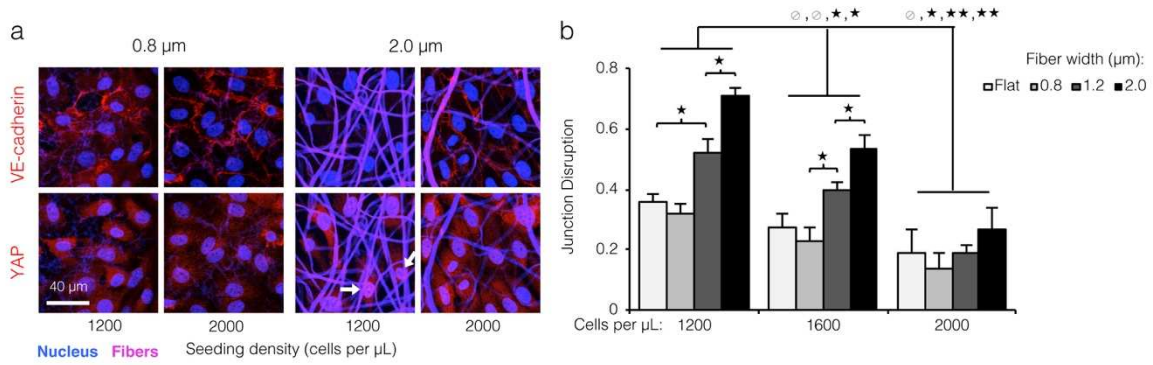

Figure S12. YAP nuclear translocation on topographically varied ELP matrices is dependent on VE-cadherin disruption. a) Confocal images of ECs cultured on varied width ELP matrices at varying cell density (low = 1200 cells per µL, high = 2000 cells per µL) and stained for nuclei (blue) and VE-cadherin (top panels, red) or YAP (bottom panels, red). Fibers shown in violet. YAP nuclear translocation was observed on large fiber matrices at low cell density (white arrows) and was not observed for ECs at high cell density, regardless of topography. b) VE-cadherin junctions could be restored on topographically varied substrates by seeding ECs at higher density. (* $p < 0.05$, ** $p < 0.01$)

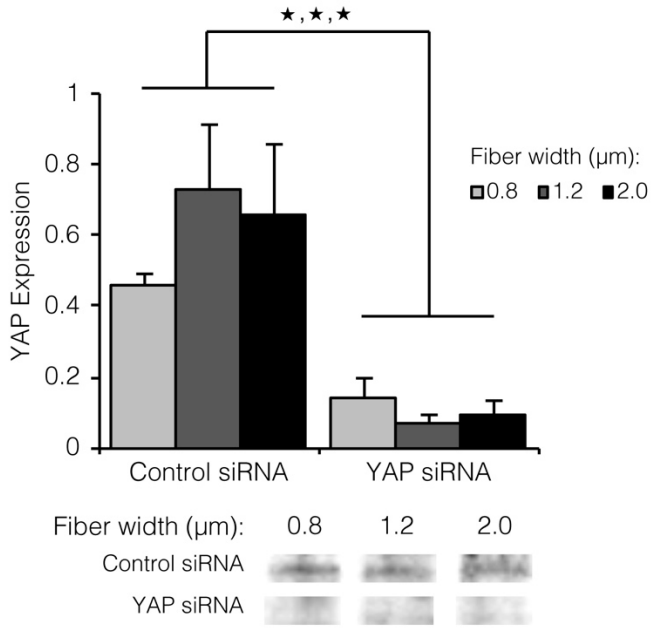

Figure S13. Western blot quantification demonstrating siRNA-mediated YAP knockdown. (* $p < 0.05$)

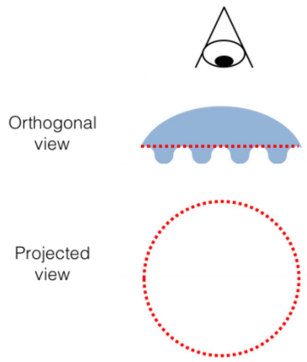

Estimate of changes in total cell surface area due to potential deformation around topographical features: To assess if the observed decrease in *projected* cell spread area with increasing topographical variation (**Figure 2d and 4c**) might be attributable to increased *basolateral* cell surface area at the fibrous interface and hence perhaps a constant *total* cell surface area, we consider a simplified model of cell-fiber interactions (shown above) with constant cell volume. We approximate an EC deforming over electrospun ELP fibers as a flattened sphere on a sinusoidal patterned substrate. We quantified the basolateral surface area for the fabrics with the greatest topographical variation (2.0-μm wide fibers) and the least topographical variation (0.8-μm wide fibers). This was achieved by summing the length of cell-fiber contact across a series of x-z/y-z orthogonal projections (3 series per fiber condition, 20 cells per series, 1-μm step size). For the 0.8- and 2.0-μm fabrics, this analysis yielded basolateral surface areas of 268 ± 13.6 μm^2 and 340 ± 11.7 μm^2, respectively (mean ± S.E.), for a difference of ~72 μm^2. While not insignificant, this value is not large enough to account for the ~270 μm^2 observed difference in projected cell spread area between the 0.8- and 2.0-μm fabrics (**Figure 2d and 4c**). Thus, trends in projected cell spread area are not entirely attributable to increased basolateral surface area and are also a result of cytoskeletal rearrangement (**Figure 2b**) and hence altered contractility on more topographically varied substrates, consistent with the observed differences seen in other experimental data sets comparing VE-cadherin organization (**Figure 2c**), cell migration (**Figure 3**), YAP localization (**Figure 5**) and cell proliferation (**Figure 6**) on substrates of varied topographical features.